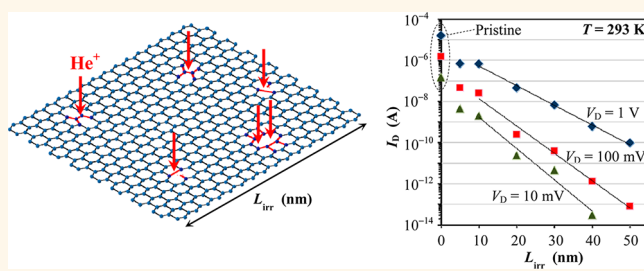


# Conduction Tuning of Graphene Based on Defect-Induced Localization

Shu Nakaharai,<sup>†,\*</sup> Tomohiko Iijima,<sup>‡</sup> Shinichi Ogawa,<sup>§</sup> Shingo Suzuki,<sup>†</sup> Song-Lin Li,<sup>†</sup> Kazuhito Tsukagoshi,<sup>†</sup> Shintaro Sato,<sup>†,\*</sup> and Naoki Yokoyama<sup>†</sup>

<sup>†</sup>Green Nanoelectronics Center (GNC), <sup>‡</sup>Innovation Center for Advanced Nanotechnology (ICAN), and <sup>§</sup>Nanoelectronics Research Institute (NeRI), National Institute of Advanced Industrial Science and Technology (AIST), 16-1 Onogawa, Tsukuba 305-8569, Japan, and <sup>†</sup>International Center for Materials Nanoarchitectonics (WPI-MANA), National Institute for Materials Science (NIMS), 1-1 Namiki, Tsukuba 305-0044, Japan

**ABSTRACT** The conduction properties of graphene were tuned by tailoring the lattice by using an accelerated helium ion beam to embed low-density defects in the lattice. The density of the embedded defects was estimated to be 2–3 orders of magnitude lower than that of carbon atoms, and they functionalized a graphene sheet in a more stable manner than chemical surface modifications can do. Current modulation through back gate biasing was demonstrated at room temperature with a current on–off ratio of 2 orders of magnitude, and the activation energy of the thermally activated transport regime was evaluated. The exponential dependence of the current on the length of the functionalized region in graphene suggested that conduction tuning is possible through strong localization of carriers at sites induced by a sparsely distributed random potential modulation.



**KEYWORDS:** graphene · carrier transport · ion irradiation · defect · helium ion microscope · transport gap · strong localization

Graphene, a two-dimensional sheet of carbon atoms,<sup>1–3</sup> has attracted the attention of scientists and engineers mainly because of its unique two-dimensional (2D) electron system. For electronics in the post-silicon scaling era, graphene is expected to be one of the main building blocks for electronics in stacks of genuine 2D atomically thin films. For this purpose, the carrier transport properties will have to be able to be modified because the lack of a band gap in graphene makes it hard to control the conductivity by electrostatic gating, and so far, this has been an obstacle to the application of graphene to logic circuits.<sup>4</sup> Chemical functionalization<sup>5,6</sup> is one of the prospective methods for transport tuning in a graphene as a sheet, which includes graphene oxide (GO),<sup>7–16</sup> hydrogenated graphene (graphane),<sup>17–25</sup> chlorinated graphene,<sup>26–29</sup> fluorinated graphene,<sup>30–35</sup> and attaching other species to the graphene with the surface.<sup>36–41</sup> These chemical surface modification techniques functionalize graphene by locally modulating the potential of the 2D electron system, and in some cases, the attached dopants work as short-range disorders for carriers.

Similar effects can be expected by embedding low-density defects in graphene;<sup>42–44</sup> this would modify transport properties via sparsely distributed local potential modulations.<sup>44–55</sup> Some researchers have argued that the mechanism of such a modification is the opening of the energy band gap,<sup>9–11,19–22,27–34,39,40,45</sup> while others have suggested it is the emergence of strongly localized states of 2D carriers.<sup>12–16,23–25,35,41,46–51</sup> From an engineering viewpoint, lattice modulation by embedding low-density defects would be better than chemical functionalization because the dopant atoms on graphene are usually unstable because of migration or desorption occurring during the chemical or heat treatments of the fabrication process. In contrast, embedded defects are free from such instability because they require a large energy (typically more than several electronvolts) to move.<sup>42</sup> Control of the transport properties by gate biasing, however, has not yet been realized in functionalized graphene to an extent that it can be applicable to electronics.

In this paper, we functionalized graphene by modulating the lattice structure with an accelerated helium ion beam. The ion doses

\* Address correspondence to shu-nakaharai@aist.go.jp, shintaro.sato@aist.go.jp.

Received for review October 19, 2012 and accepted June 20, 2013.

Published online June 20, 2013  
10.1021/nn401992q

© 2013 American Chemical Society

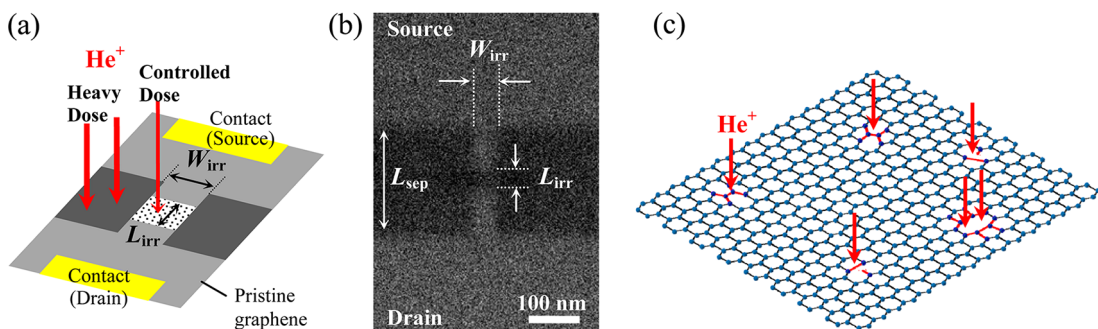


Figure 1. (a) Schematic illustration of the fabricated device. The central part with length  $L_{\text{irr}}$  and width  $W_{\text{irr}}$  is irradiated with controlled helium ion doses of  $2.2 \times 10^{15}$  to  $1.3 \times 10^{16}$  ions/cm $^2$ , which induces defects with the densities of 0.2 to 1.3%. Outside of this part, graphene regions with source and drain contacts are separated by heavily dosed ( $1.3 \times 10^{16}$  ions/cm $^2$ ) regions with the length of  $L_{\text{sep}} = 200$  nm. This heavy ion dose is large enough to electrically separate the graphene regions of the source and drain, and hence, the conductance between source and drain is dominated by the resistance of the central part of  $W_{\text{irr}} \times L_{\text{irr}}$  with the controlled dose. (b) Helium ion micrograph of a fabricated device with  $W_{\text{irr}} = 50$  nm,  $L_{\text{irr}} = 30$  nm, and  $L_{\text{sep}} = 200$  nm. Dark regions were irradiated with the helium ion beam. (c) Schematic of typical distribution of defects with the density of 1%, including Stone-Wales defects, monovacancies, and divacancies.

tailored graphene by embedding point imperfections at the density of 2–3 orders of magnitude lower than that of the carbon atoms in the graphene sheet; these imperfections acted as sparsely distributed local potential modulations for the 2D electron system in graphene (Figure 1). We found that carrier transport in functionalized graphene could be modulated by back gate biasing with an on–off ratio of current of 2 orders of magnitude at room temperature in a sample with an optimized ion dose. We also found that the conductance decayed exponentially as the size of functionalized graphene area increased, implying that the transport was not governed by the Schottky barrier formed at the junction between functionalized and pristine graphene regions. This indicates that the carrier transport in the functionalized graphene is dominated by strong localization of carriers even at room temperature, rather than being due to an opening of the band gap.

## RESULTS AND DISCUSSION

As the defect density increases,  $I_D$  rapidly decays and the plateau at zero bias becomes pronounced, as shown in a series of  $I_D$ – $V_D$  curves for different defect density at room temperature (Figure 2a,b). The devices used in these measurements had a fixed  $L_{\text{irr}}$  of 30 nm and  $W_{\text{irr}}$  of 50 nm and were processed together on a single chip. The exponential decay of the current with increasing defect density (Figure 2c) implies that the embedded low-density defects induce a metal–insulator transition. In order to investigate the crystal structure change by the ion irradiation, we took Raman spectra of five samples with different defect densities at the excitation laser wavelength of 488 nm. The obtained spectra shown in Figure 2d indicate that the D mode peak, which reflects the existence of defects, is enhanced as the number of defects increases, while the G mode peak is apparent even at high defect densities, suggesting that the honeycomb structure of the carbon atom network remains even when the graphene is

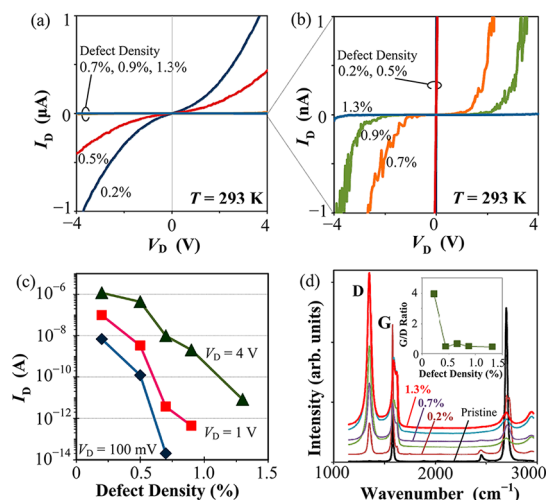
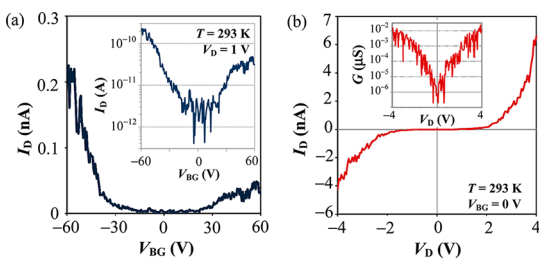


Figure 2. (a) Drain bias ( $V_D$ ) dependence of the drain current ( $I_D$ ) at room temperature in a device with  $W_{\text{irr}} = 50$  nm and  $L_{\text{irr}} = 30$  nm for different defect densities of 0.2, 0.5, 0.7, 0.9, and 1.3% in the current range of 1  $\mu$ A. (b) Enlargement of the plot of (a) in the current range of 1 nA. The current decays rapidly as the defect density increases, and simultaneously, the nonlinear behavior of  $I_D$ – $V_D$  curves becomes pronounced. (c) Defect density dependence of  $I_D$  at different  $V_D$  values of 100 mV, 1 V, and 4 V. (d) Raman spectra of pristine and helium ion irradiated graphene with defect densities of 0.2, 0.5, 0.7, 0.9, and 1.3%. The defect density dependence of the G/D ratio is shown in the inset.

almost insulating. The saturating behavior of the G/D ratio shown in the inset of Figure 2d is consistent with that in graphene with  $\text{Ar}^+$  bombardment.<sup>56</sup> These results suggest that the exponential decay of  $I_D$  with the defect density occurs without any essential change in the crystalline structure.

The modulation of  $I_D$  by  $V_{\text{BG}}$  was demonstrated at room temperature in a sample with a defect density of 0.9% (Figure 3a). Here, the drain current exhibits strong suppression around zero bias of the back gate, and its logarithmic plot in the inset indicates a current on–off ratio of 2 orders of magnitude. Figure 3b shows the  $I_D$ – $V_D$  curve of the same sample, and the inset shows



**Figure 3.** (a) Back gate bias ( $V_{BG}$ ) dependence of the drain current ( $I_D$ ) with a fixed drain bias ( $V_D$ ) of 1 V at room temperature in a sample with a defect density of 0.9%. The logarithmic-scale plot in the inset shows an on-off ratio of 2 orders of magnitude. (b)  $V_D$  dependence of  $I_D$  at room temperature of the same sample shown in (a) and its differential conductance in the inset.

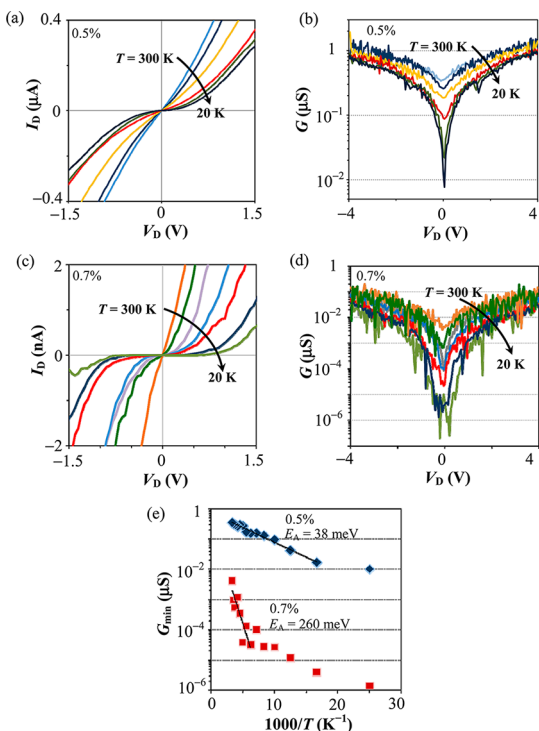


**Figure 4.** (a) Drain bias ( $V_D$ ) dependence of drain current ( $I_D$ ) in a sample with a defect density of 0.5% at temperatures of  $T = 300, 250, 200, 180, 160, 140, 120, 100, 80, 60$ , and 20 K. The back gate bias ( $V_{BG}$ ) is zero. (b) Differential conductance ( $G$ ) derived from the plots shown in (a). (c)  $I_D - V_D$  curves in a sample with a defect density of 0.7% at  $T = 300, 240, 200, 180, 160, 140, 120, 100, 80, 60$ , and 20 K, and (d) differential conductance. (e) Temperature dependence of the conductance minimum ( $G_{min}$ ) at  $V_D = 0$  V in samples with defect densities of 0.5 and 0.7%. The activation energies ( $E_A$ ) are extracted from these plots as 38 and 260 meV for samples with defect densities of 0.5 and 0.7%.

the  $V_D$  dependence of the differential conductance  $G = |dI_D/dV_D|$ . The plateau of the  $I_D - V_D$  curve and the conductance drop at  $V_D = 0$  V are evidence of strong suppression of carrier transport properties around the charge neutrality point.

To investigate the nature of the strong suppression of conductance around the charge neutrality point, we plotted the temperature dependence of  $I_D - V_D$  and  $G - V_D$  characteristics (Figure 4a,b, respectively) of a

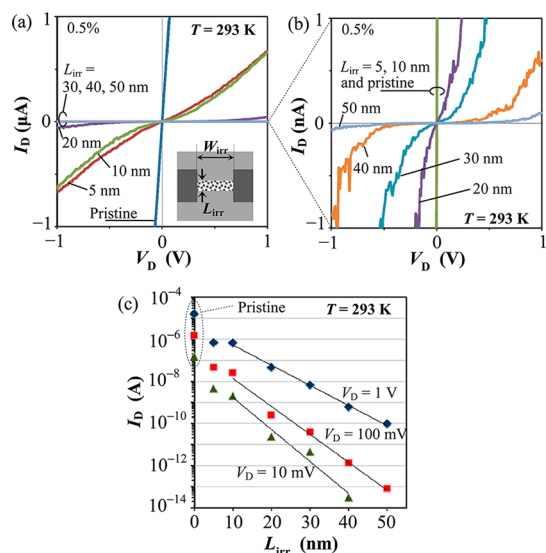


**Figure 5.** (a) Drain bias ( $V_D$ ) dependence of drain current ( $I_D$ ) at room temperature in devices fabricated with  $L_{irr} = 0, 5, 10, 20, 30, 40, 50$  nm, fixed  $W_{irr} = 200$  nm, and a defect density of 0.5% in a current range of  $1 \mu\text{A}$ . (b) Enlargement of the plot of (a) in the current range of  $1 \text{nA}$ . The current decays rapidly as  $L_{irr}$  increases, and simultaneously, the nonlinear behavior of  $I_D - V_D$  curves becomes pronounced. (c)  $L_{irr}$  dependence of  $I_D$  at different  $V_D$  values of  $10 \text{ mV}$ ,  $100 \text{ mV}$ , and  $1 \text{ V}$ .

sample with a defect density of 0.5% at temperatures between 20 and 300 K. As the temperature decreases, the plateau of  $I_D$  around  $V_D = 0$  V becomes more pronounced, and hence, the conductance minimum,  $G_{min}$ , decreases rapidly. In contrast,  $G$  at large  $V_D$  values shows a much smaller change than in the  $V_D = 0$  V case. Another sample with a larger defect density (0.7%) shows a more abrupt change in the plateau of  $I_D$  and a dip in  $G$  with decreasing temperature (Figure 4c,d). The temperature dependence of  $G_{min}$  is plotted in Figure 4e as an Arrhenius plot. In each sample with higher or lower defect densities, it is apparent that  $G_{min}$  fits the thermally activated transport scheme at high temperatures:

$$G_{min} \propto \exp(-E_A/2k_B T) \quad (1)$$

where  $k_B$  is the Boltzmann's constant and  $E_A$  is the activation energy.  $E_A$  was derived from these plots according to formula 1; it was 38 and 260 meV for the samples with defect densities of 0.5 and 0.7%, respectively. It is notable that  $E_A$  was quite sensitive to the defect density. On the other hand, at lower temperatures, transport is likely dominated by the variable range hopping, which can be seen in the deviation of  $G_{min}$  from the Arrhenius fitting curve. Such temperature-dependent features of the conductance are commonly found in conductors with strong localization sites.

To gain a better understanding of the transport properties of our functionalized graphene, we investigated the dependence of the current on the irradiated region length in samples with a defect density of 0.5% and  $W_{irr}$  of 200 nm at room temperature of 293 K (Figure 5a,b). The  $L_{irr}$  dependence of  $I_D$  summarized in

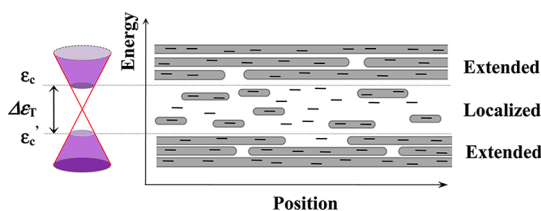


**Figure 6.** Schematic illustration of localized and extended carrier states, transport gap ( $\Delta\epsilon_r$ ) and mobility edges ( $\epsilon_c$  and  $\epsilon_c'$ ). Black short line segments represent the localization sites, and gray regions are where carriers exist. Within the transport gap, where the density of states is lower than that out of the gap, carriers are isolated from each other due to the low density of carriers. On the other hand, outside the transport gap, where the density of states is higher, the localized carriers tend to overlap and extend over the whole sample, resulting in carrier conductance through the sample. The mobility edge is the energy level separating these two regimes of localized and extended states.

Figure 5c for  $V_D = 10$  mV, 100 mV, and 1 V indicates that  $I_D$  decays as an exponential function of  $L_{irr}$  when  $L_{irr}$  is longer than 10 nm. This result rules out a model based on the thermionic emission<sup>57</sup> in which ion irradiation opens the band gap. In such a model, the Schottky barrier at the junction between the irradiated and pristine graphene regions dominates the conduction through the whole sample; as is commonly discussed in the cases of chemically functionalized graphene,<sup>9,12</sup> the current is almost independent of the channel length in the thermionic emission model with a semiconducting band gap. Instead, it is more reasonable to consider strong localization of carriers due to interference of waves which are scattered at defect sites. In the strong localization scheme, the transport gap appears around the charge neutrality point where the density of states is relatively low, and hence, the localized carriers are separated from each other (Figure 6). This feature gives rise to the transport modulation by back gate bias shown in Figure 3a by moving the Fermi level into or out of the transport gap.

The mechanism whereby strongly localized states are induced by randomly distributed low-density defects should be discussed on the basis of a strong (Anderson) localization scheme.<sup>15,16,25,51,58,59</sup> For this effect to happen in our case of irradiated graphene, phase coherence must be retained even at room temperature. In usual conductors, phase coherence will be thermally destroyed by the phonon scattering, while in the case of graphene, since the electron–phonon coupling is extremely weak,<sup>60</sup> thermal dephasing is supposed to be suppressed, enabling strong localization to be sustained up to room temperature.<sup>51</sup> The density of defects in the graphene crystal required for a transition to the strongly localized state has been predicted to be around 1%,<sup>51</sup> which shows good agreement with our experimental data shown in Figure 2. Experimentally, the densities of other scatterers attached on graphene such as oxygen<sup>16</sup> or hydrogen<sup>25</sup> for the metal–insulator transition have also been

reported, which are consistent with our defect density. In the case of graphene oxide,<sup>16</sup> the coverage of epoxide scatterers, which gives rise to the metal–insulator transition, has been found to be from 0.1 to 4%. Furthermore, in hydrogenated graphene (graphane),<sup>25</sup> a transition to the strongly localized state at the hydrogen density on the order of 0.1% has been reported. These densities of scatters are consistent with our result. Although the fundamental nature of the localized state at room temperature must be proved experimentally and theoretically, our results showing a defect-mediated metal–insulator transition and the exponential dependence of carrier transport on length are straightforward evidence of Anderson-like strongly localized states in disordered graphene.

For application of our helium ion irradiated graphene to transistors especially in high-performance large-scale integrated circuits, the low on-state current could be an obstacle. For overcoming the low current issue, we present some methods to increase the current; one of them is to make the channel wider in order to avoid the confinement and edge scattering effects (see Supporting Information). Also, the on-state current would be enhanced if the channel length becomes shorter than typically 50 nm, as indicated in Figure 5c. In this case, since the channel length dependence of current is *exponential*, the current flowing in the channel increases drastically by shrinking the channel length. For aggressively scaled graphene transistors with a very short channel, we have proposed the novel concept of a dual-gated graphene transistor, in which the graphene region between a pair of top gates has an energy gap (band gap or transport gap) and the carrier conduction is controlled by raising up or pulling down the bands of graphene under the top gates.<sup>61</sup> This structure can elude the allowance to align the top gate to the graphene channel with an energy gap in the conventional transistor structure, and hence the channel length of graphene with an energy gap could be the same as the distance between top gates if a self-aligned channel fabrication process to the gates is employed (see Supporting Information).

## CONCLUSIONS

In conclusion, we experimentally investigated the modification of the electrical properties of graphene by tailoring graphene's lattice structure by embedding low-density defects to induce local potential modulation of the electron system. The density of embedded defects was estimated to be 2–3 orders of magnitude lower than the density of carbon atoms in the graphene lattice, and Raman spectroscopy confirmed that most of the hexagonal structure of the graphene lattice remained even when the graphene was insulating. We demonstrated nonlinear  $I_D$ – $V_D$  characteristics and  $I_D$  modulation by  $V_{BG}$  with an on–off ratio of 2 orders of magnitude in functionalized graphene at

room temperature. The activation energy of the thermally activated transport scheme was estimated from the temperature dependence of the conductance. We also found that the conductance decays exponentially as the irradiated region length increases, suggesting that the carrier transport is dominated by strong localization of carriers at the localization sites induced by the defects. These results will contribute not only

to our basic understanding of carrier transport in functionalized graphene but also to the development of graphene electronics by offering a functionalization process of graphene as a large sheet with ion irradiation. This would enable wafer-scale mass production of graphene devices, and these features will be important for future electronics on atomically thin 2D functional films.

## METHODS

Single-layer graphene flakes were mechanically exfoliated from a crystal of highly oriented pyrolytic graphite (HOPG) using adhesive tape and deposited on a silicon wafer with a 285 nm thick surface thermal oxide layer. The substrate was a highly doped p-type silicon with boron impurities ( $>10^{18} \text{ cm}^{-3}$ ) which was used as a back gate electrode. The locations and the number of graphene layers were identified by optical contrast<sup>62</sup> using an optical microscope. Source and drain contacts were formed by electron-beam lithography using poly(methyl methacrylate) (PMMA) resist, and metal contacts of Ti/Au (5/30 nm) were thermally evaporated and then lifted off. The contact resistance,  $R$ , of the fabricated devices was checked before the ion irradiation process by observing the back gate bias,  $V_{BG}$ , dependence of  $I_D$  in order to select devices with  $R$  values lower than 1 k $\Omega$  and a Dirac peak position in the  $R$ – $V_{BG}$  curve within 2 V from the zero of  $V_{BG}$ . The graphene surface between the source and drain contacts was irradiated with a helium ion beam by scanning the beam in a helium ion microscope at the acceleration voltage of 30 kV, a technique that was first used for etching graphene by Lemme<sup>63</sup> and Bell.<sup>64</sup> In this process, the helium ion beam was focused at the graphene surface with the beam diameter less than 1 nm, enabling ultra-high-resolution fabrication. Graphene devices for investigating electrical properties of helium ion irradiated graphene were fabricated as shown in Figure 1. A central rectangular region with a width,  $W_{irr}$ , and a length,  $L_{irr}$ , was exposed to the helium ion beam with controlled doses from  $2.2 \times 10^{15}$  to  $1.3 \times 10^{16} \text{ ions/cm}^2$  (Figure 1a). Here,  $L_{irr}$  ranged from 5 to 50 nm, and  $W_{irr}$  was 50 or 200 nm. This region will be referred to as “channel” in this article. The graphene regions outside of the channel were irradiated with a heavy dose of  $1.3 \times 10^{16} \text{ ions/cm}^2$ , in order to turn this region insulating, with a separation length,  $L_{sep}$ , of at least 200 nm. Thus, the source and drain regions were connected only by the channel. The insulation of the heavily dosed graphene was confirmed using a sample with source and drain regions separated by the heavily dosed graphene, which exhibited the current across the heavily dosed region much lower than 1 pA at a  $V_D$  up to 10 V. The helium ion micrograph in Figure 1b shows a device with  $W_{irr} = 50 \text{ nm}$ ,  $L_{irr} = 30 \text{ nm}$ , and  $L_{sep} = 200 \text{ nm}$ . After each ion irradiation process, we applied an electron shower to graphene in order to neutralize the trapped positive charges due to the introduced helium ions. Electric properties in the irradiated graphene were obtained by two-terminal DC measurements of the drain current,  $I_D$ , by sweeping the drain bias,  $V_D$ , or the back gate bias,  $V_{BG}$ , at temperatures from 20 to 300 K using a cryogenic probe station.

The primary effect of the helium ion beam is to embed point defects in the honeycomb lattice of graphene (Figure 1c), and it has been predicted theoretically that the ion bombardment generates point defects in graphene at the ion acceleration voltage of 30 kV.<sup>65,66</sup> These point defects include monovacancy, divacancy, and/or Stone–Wales-type ones,<sup>43</sup> and the possibility of existence of these point defects was directly proved in graphene by the observations by TEM<sup>67,68</sup> or STM,<sup>44</sup> while it has not yet been confirmed in our ion irradiated graphene. According to a numerical calculation, the percentage of helium ions which interact with carbon atoms of the graphene sheet is only 0.4%,<sup>64</sup> taking into account the helium ion doses of  $2.2 \times 10^{15}$  to  $1.3 \times 10^{16} \text{ ions/cm}^2$  and a carbon atom density in a

graphene sheet of  $3.8 \times 10^{15} \text{ cm}^{-2}$ , the density of embedded point defects ranges from 0.2 to 1.3%, corresponding to the number of defects for every 100 carbon atoms. The majority of helium ions are supposed to reach the silicon substrate, according to the calculation.<sup>64</sup> These ions trapped in the silicon substrate, however, did not have any noticeable effect on the electric properties of the graphene device. The positive charges of helium ions, which should be immediately neutralized since the substrate is grounded, could work as donor dopant for silicon, but the silicon substrate was already highly (degenerately) doped with boron ( $>10^{18} \text{ cm}^{-3}$ ), meaning that the counter-doping effect of helium ions is negligible. For the ions trapped near the surface, on the other hand, the positive charges were neutralized by electron shower treatment just after the ion irradiation. For these reasons, the effects of positively charged helium ions are negligible.

*Conflict of Interest:* The authors declare no competing financial interest.

*Acknowledgment.* The authors are grateful to M. Ohfuchi and T. Usuki for fruitful discussions. This research is granted by the Japan Society for the Promotion of Science (JSPS) through the Funding Program for World-Leading Innovative R&D on Science and Technology (FIRST Program), initiated by the Council for Science and Technology Policy (CSTP).

*Supporting Information Available:* Supplementary data of additional experiments of on-state current enhancement. This material is available free of charge via the Internet at <http://pubs.acs.org>.

## REFERENCES AND NOTES

- Novoselov, K. S.; Geim, A. K.; Morozov, S. V.; Jiang, D.; Zhang, Y.; Dubonos, S. V.; Grigorieva, I. V.; Firsov, A. A. Electric Field Effect in Atomically Thin Carbon Films. *Science* **2004**, *306*, 666–669.
- Novoselov, K. S.; Geim, A. K.; Morozov, S. V.; Jiang, D.; Katsnelson, M. I.; Grigorieva, I. V. S.; Dubonos, V.; Firsov, A. A. Two Dimensional Gas of Massless Dirac Fermions in Graphene. *Nature* **2005**, *438*, 197–200.
- Zhang, Y.; Tan, Y.-W.; Stormer, H. L.; Kim, P. Experimental Observation of the Quantum Hall Effect and Berry’s Phase in Graphene. *Nature* **2005**, *438*, 201–204.
- Schwierz, F. Graphene Transistors. *Nat. Nanotechnol.* **2010**, *5*, 487–496.
- Boukhvalov, D. W.; Katsnelson, M. I. Chemical Functionalization of Graphene with Defects. *Nano Lett.* **2008**, *8*, 4373–4379.
- Boukhvalov, D. W.; Katsnelson, M. I. Chemical Functionalization of Graphene. *J. Phys.: Condens. Matter* **2009**, *21*, 344205.
- Gilje, S.; Han, S.; Wang, M.; Wang, K. L.; Kaner, R. B. A Chemical Route to Graphene for Device Applications. *Nano Lett.* **2007**, *7*, 3394–3398.
- Tung, V. C.; Allen, M. J.; Yang, Y.; Kaner, R. B. High-Throughput Solution Processing of Large-Scale Graphene. *Nat. Nanotechnol.* **2008**, *4*, 25–29.
- Wu, X.; Sprinkle, M.; Li, X.; Ming, F.; Berger, C.; de Heer, W. A. Epitaxial-Graphene/Graphene-Oxide Junction: An Essential Step towards Epitaxial Graphene Electronics. *Phys. Rev. Lett.* **2008**, *101*, 026801.

10. Fujii, S.; Enoki, T. Cutting of Oxidized Graphene into Nanosized Pieces. *J. Am. Chem. Soc.* **2010**, *132*, 10034–10041.
11. Guo, L.; Shao, R.-Q.; Zhang, Y.-L.; Jiang, H.-B.; Li, X.-B.; Xie, S.-Y.; Xu, B.-B.; Chen, Q.-D.; Song, J.-F.; Sun, H.-B. Bandgap Tailoring and Synchronous Microdevices Patterning of Graphene Oxides. *J. Phys. Chem. C* **2012**, *116*, 3594–3599.
12. Masubuchi, S.; Arai, M.; Machida, T. Atomic Force Microscopy Based Tunable Local Anodic Oxidation of Graphene. *Nano Lett.* **2011**, *11*, 4542–4546.
13. Gómez-Navarro, C.; Weitz, R. T.; Bittner, A. M.; Scolari, M.; Mews, A.; Burghard, M.; Kern, K. Electronic Transport Properties of Individual Chemically Reduced Graphene Oxide Sheets. *Nano Lett.* **2007**, *7*, 3499–3503.
14. Yan, J.-A.; Xian, L.; Chou, M. Y. Structural and Electronic Properties of Oxidized Graphene. *Phys. Rev. Lett.* **2009**, *103*, 086802.
15. Leconte, N.; Lherbier, A.; Varchon, F.; Ordejon, P.; Roche, S.; Charlier, J.-C. Quantum Transport in Chemically Modified Two-Dimensional Graphene: From Minimal Conductivity to Anderson Localization. *Phys. Rev. B* **2011**, *84*, 235420.
16. Leconte, N.; Moser, J.; Ordejón, P.; Tao, H.; Lherbier, A.; Bachtold, A.; Alsina, F.; Sotomayor Torres, C. M.; Charlier, J.-C.; Roche, S. Damaging Graphene with Ozone Treatment: A Chemically Tunable Metal Insulator Transition. *ACS Nano* **2010**, *4*, 4033–4038.
17. Elias, D. C.; Nair, R. R.; Mohiuddin, T. M. G.; Morozov, S. V.; Blake, P.; Halsall, M. P.; Ferrari, A. C.; Boukhvalov, D. W.; Katsnelson, M. I.; Geim, A. K.; et al. Control of Graphene's Properties by Reversible Hydrogenation: Evidence for Graphane. *Science* **2009**, *323*, 610–613.
18. Ryu, S.; Han, M. Y.; Maultzsch, J.; Heinz, T. F.; Kim, P.; Steigerwald, M. L.; Brus, L. E. Reversible Basal Plane Hydrogenation of Graphene. *Nano Lett.* **2008**, *8*, 4597–4602.
19. Balog, R.; Jørgensen, B.; Nilsson, L.; Andersen, M.; Rienks, E.; Bianchi, M.; Fanetti, M.; Lægsgaard, E.; Baraldi, A.; Lizzit, S.; et al. Bandgap Opening in Graphene Induced by Patterned Hydrogen Adsorption. *Nat. Mater.* **2010**, *9*, 315–319.
20. Matis, B. R.; Burgess, J. S.; Bulat, F. A.; Friedman, A. L.; Houston, B. H.; Baldwin, J. W. Surface Doping and Band Gap Tunability in Hydrogenated Graphene. *ACS Nano* **2012**, *6*, 17–22.
21. Sofo, J. O.; Chaudhari, A. S.; Barber, G. D. Graphane: A Two-Dimensional Hydrocarbon. *Phys. Rev. B* **2007**, *75*, 153401.
22. Havu, P.; Ijäs, M.; Harju, A. Hydrogenated Graphene on Silicon Dioxide Surfaces. *Phys. Rev. B* **2011**, *84*, 205423.
23. Chuang, C.; Puddy, R. K.; Lin, H.-D.; Lo, S.-T.; Chen, T.-M.; Smith, C. G.; Liang, C.-T. Experimental Evidence for Efros–Shklovskii Variable Range Hopping in Hydrogenated Graphene. *Solid State Commun.* **2012**, *152*, 905–908.
24. Bang, J.; Chang, K. J. Localization and One-Parameter Scaling in Hydrogenated Graphene. *Phys. Rev. B* **2010**, *81*, 193412.
25. Bostwick, A.; McChesney, J. L.; Emtsev, K. V.; Seyller, T.; Horn, K.; Kavan, S. D.; Rotenberg, E. Quasiparticle Transformation during a Metal–Insulator Transition in Graphene. *Phys. Rev. Lett.* **2009**, *103*, 056404.
26. Ijäs, M.; Havu, P.; Harju, A. Fracturing Graphene by Chlorination: A Theoretical Viewpoint. *Phys. Rev. B* **2012**, *85*, 035440.
27. Li, B.; Zhou, L.; Wu, D.; Peng, H.; Yan, K.; Zhou, Y.; Liu, Z. Photochemical Chlorination of Graphene. *ACS Nano* **2011**, *5*, 5957–5961.
28. Wu, J.; Xie, L.; Li, Y.; Wang, H.; Ouyang, Y.; Guo, J.; Dai, H. Controlled Chlorine Plasma Reaction for Noninvasive Graphene Doping. *J. Am. Chem. Soc.* **2011**, *133*, 19668–19671.
29. Yang, M.; Zhou, L.; Wang, J.; Liu, Z.; Liu, Z. Evolutionary Chlorination of Graphene: From Charge-Transfer Complex to Covalent Bonding and Nonbonding. *J. Phys. Chem. C* **2012**, *116*, 844–850.
30. Nair, R. R.; Ren, W.; Jalil, R.; Riaz, I.; Kravets, V. G.; Britnell, L.; Blake, P.; Schedin, F.; Mayorov, A. S.; Yuan, S.; et al. Fluorographene: A Two-Dimensional Counterpart of Teflon. *Small* **2010**, *6*, 2877–2884.
31. Cheng, S.-H.; Zou, K.; Okino, F.; Gutierrez, H. R.; Gupta, A.; Shen, N.; Eklund, P. C.; Sofo, J. O.; Zhu, J. Reversible Fluorination of Graphene: Evidence of a Two-Dimensional Wide Bandgap Semiconductor. *Phys. Rev. B* **2010**, *81*, 205435.
32. Withers, F.; Bointon, T. H.; Dubois, M.; Russo, S.; Craciun, M. F. Nanopatterning of Fluorinated Graphene by Electron Beam Irradiation. *Nano Lett.* **2011**, *11*, 3912–3916.
33. Lee, W. H.; Suk, J. W.; Chou, H.; Lee, J.; Hao, Y.; Wu, Y.; Piner, R.; Akinwande, D.; Kim, K. S.; Ruoff, R. S. Selective-Area Fluorination of Graphene with Fluoropolymer and Laser Irradiation. *Nano Lett.* **2012**, *12*, 2374–2378.
34. Leenaerts, O.; Peelaers, H.; Hernández-Nieves, A. D.; Partoens, B.; Peeters, F. M. First-Principles Investigation of Graphene Fluoride and Graphane. *Phys. Rev. B* **2010**, *82*, 195436.
35. Withers, F.; Dubois, M.; Savchenko, A. K. Electron Properties of Fluorinated Single-Layer Graphene Transistors. *Phys. Rev. B* **2010**, *82*, 073403.
36. Liu, H.; Lee, J. Y. Electric Field Effects on the Adsorption of CO on a Graphene Nanodot and the Healing Mechanism of a Vacancy in a Graphene Nanodot. *J. Phys. Chem. C* **2012**, *116*, 3034–3038.
37. Sun, J. T.; Lu, Y. H.; Chen, W.; Feng, Y. P.; Wee, A. T. S. Linear Tuning of Charge Carriers in Graphene by Organic Molecules and Charge-Transfer Complexes. *Phys. Rev. B* **2010**, *81*, 155403.
38. Englert, J. M.; Dotzer, C.; Yang, G.; Schmid, M.; Papp, C.; Gottfried, J. M.; Steinrück, H.-P.; Spiecker, E.; Hauke, F.; Hirsch, A. Covalent Bulk Functionalization of Graphene. *Nat. Chem.* **2011**, *3*, 279–286.
39. Niyogi, S.; Belyarova, E.; Itkis, M. E.; Zhang, H.; Shepperd, K.; Hicks, J.; Sprinkle, M.; Berger, C.; Lau, C. N.; deHeer, W. A.; et al. Spectroscopy of Covalently Functionalized Graphene. *Nano Lett.* **2010**, *10*, 4061–4066.
40. Zhang, H.; Belyarova, E.; Huang, J.-W.; Zhao, Z.; Bao, W.; Wang, F.; Haddon, R. C.; Lau, C. N. Aryl Functionalization as a Route to Band Gap Engineering in Single Layer Graphene Devices. *Nano Lett.* **2011**, *11*, 4047–4051.
41. Joucken, F.; Tison, Y.; Lagoute, J.; Dumont, J.; Cabosart, D.; Zheng, B.; Repain, V.; Chacon, C.; Girard, Y.; Botello-Méndez, A. R.; et al. Localized State and Charge Transfer in Nitrogen-Doped Graphene. *Phys. Rev. B* **2012**, *85*, 161408.
42. Banhart, F.; Kotakoski, J.; Krasheninnikov, A. V. Structural Defects in Graphene. *ACS Nano* **2011**, *5*, 26–41.
43. Stone, A.; Wales, D. Theoretical Studies of Icosahedral C<sub>60</sub> and Some Related Species. *Chem. Phys. Lett.* **1986**, *128*, 501–503.
44. Ugeda, M. M.; Brihuega, I.; Hiebel, F.; Mallet, P.; Veuillen, J.-Y.; Gómez-Rodríguez, J. M.; Ynduráin, F. Electronic and Structural Characterization of Divacancies in Irradiated Graphene. *Phys. Rev. B* **2012**, *85*, 121402.
45. Peng, X.; Ahuja, R. Symmetry Breaking Induced Bandgap in Epitaxial Graphene Layers on SiC. *Nano Lett.* **2008**, *8*, 4464–4468.
46. Aleiner, I. L.; Efetov, K. B. Effect of Disorder on Transport in Graphene. *Phys. Rev. Lett.* **2006**, *97*, 236801.
47. Xing, Y.; Zhang, L.; Wang, J. Topological Anderson Insulator Phenomena. *Phys. Rev. B* **2011**, *84*, 035110.
48. Amini, M.; Jafari, S. A.; Shahbazi, F. Anderson Transition in Disordered Graphene. *Eur. Phys. Lett.* **2009**, *87*, 37002.
49. Ryu, S.; Mudry, C.; Ludwig, A. W. W.; Furusaki, A. Global Phase Diagram of Two-Dimensional Dirac Fermions in Random Potentials. *Phys. Rev. B* **2012**, *85*, 235115.
50. Lherbier, A.; Biel, B.; Niquet, Y.-M.; Roche, S. Transport Length Scales in Disordered Graphene-Based Materials: Strong Localization Regimes and Dimensionality Effects. *Phys. Rev. Lett.* **2008**, *100*, 036803.
51. Lherbier, A.; Dubois, S. M.-M.; Declerck, X.; Niquet, Y.-M.; Roche, S.; Charlier, J.-C. Transport Properties of Graphene Containing Structural Defects. *Phys. Rev. B* **2012**, *86*, 075402.
52. Adam, S.; Cho, S.; Fuhrer, M. S.; Das Sarma, S. Density Inhomogeneity Driven Percolation Metal–Insulator Transition

and Dimensional Crossover in Graphene Nanoribbons. *Phys. Rev. Lett.* **2008**, *101*, 046404.

53. Tapasztó, L.; Dobrik, G.; Nemes-Incze, P.; Vertes, G.; Lambin, Ph.; Biró, L. P. Tuning the Electronic Structure of Graphene by Ion Irradiation. *Phys. Rev. B* **2008**, *78*, 233407.
54. Chen, J.-H.; Cullen, W. G.; Jang, C.; Fuhrer, M. S.; Williams, E. D. Defect Scattering in Graphene. *Phys. Rev. Lett.* **2009**, *102*, 236805.
55. Zhou, Y.-B.; Liao, Z.-M.; Wang, Y.-F.; Duesberg, G. S.; Xu, J.; Fu, Q.; Wu, X.-S.; Yu, D.-P. Ion Irradiation Induced Structural and Electrical Transition in Graphene. *J. Chem. Phys.* **2010**, *133*, 234703.
56. Cançado, L. G.; Jorio, A.; Martins Ferreira, E. H.; Stavale, F.; Achete, C. A.; Capaz, R. B.; Moutinho, M. V. O.; Lombardo, A.; Kulmala, T. S.; Ferrari, A. C. Quantifying Defects in Graphene via Raman Spectroscopy at Different Excitation Energies. *Nano Lett.* **2011**, *11*, 3190–3196.
57. Anwar, A.; Nabot, B.; Culp, J.; Castro, F. Effects of Electron Confinement on Thermionic Emission Current in a Modulation Doped Heterostructure. *J. Appl. Phys.* **1999**, *85*, 2663–2666.
58. Ponomarenko, L. A.; Geim, A. K.; Zhukov, A. A.; Jalil, R.; Morozov, S. V.; Novoselov, K. S.; Grigorieva, I. V.; Hill, E. H.; Cheianov, V. V.; Fal'ko, V. I.; et al. Tunable Metal–Insulator Transition in Double-Layer Graphene Heterostructures. *Nat. Phys.* **2011**, *7*, 958–961.
59. Gómez-Navarro, C.; Pablo, P. J.; Gómez-Herrero, J.; Biel, B.; García-Vidal, F. J.; Rubio, A.; Flores, F. Tuning the Conductance of Single-Walled Carbon Nanotubes by Ion Irradiation in the Anderson Localization Regime. *Nat. Mater.* **2005**, *4*, 534–539.
60. Morozov, S. V.; Novoselov, K. S.; Katsnelson, M. I.; Schedin, F.; Elias, D. C.; Jaszczak, J. A.; Geim, A. K. Giant Intrinsic Carrier Mobilities in Graphene and Its Bilayer. *Phys. Rev. Lett.* **2008**, *100*, 016602.
61. Nakaharai, S.; Iijima, T.; Ogawa, S.; Miyazaki, H.; Li, S.-L.; Tsukagoshi, K.; Sato, S.; Yokoyama, N. Gate-Controlled P–I–N Junction Switching Device with Graphene Nanoribbon. *Appl. Phys. Exp.* **2012**, *5*, 015101.
62. Hiura, H.; Miyazaki, H.; Tsukagoshi, K. Determination of the Number of Graphene Layers: Discrete Distribution of the Secondary Electron Intensity Stemming from Individual Graphene Layers. *Appl. Phys. Exp.* **2010**, *3*, 095101.
63. Lemme, M. C.; Bell, D. C.; Williams, J. R.; Stern, L. A.; Baugher, B. W. H.; Jarillo-Herrero, P.; Marcus, C. M. Etching of Graphene Devices with a Helium Ion Beam. *ACS Nano* **2009**, *3*, 2674–2676.
64. Bell, D. C.; Lemme, M. C.; Stern, L. A.; Williams, J. R.; Marcus, C. M. Precision Cutting and Patterning of Graphene with Helium Ions. *Nanotechnology* **2009**, *20*, 455301.
65. Lehtinen, O.; Kotakoski, J.; Krasheninnikov, A. V.; Tolvanen, A.; Nordlund, K.; Keinonen, J. Effects of Ion Bombardment on a Two-Dimensional Target: Atomistic Simulations of Graphene Irradiation. *Phys. Rev. B* **2010**, *81*, 153401.
66. Åhlgren, E. H.; Kotakoski, J.; Lehtinen, O.; Krasheninnikov, A. V. Ion Irradiation Tolerance of Graphene as Studied by Atomistic Simulations. *Appl. Phys. Lett.* **2012**, *100*, 233108.
67. Hashimoto, A.; Suenaga, K.; Glotter, A.; Urita, K.; Iijima, S. Direct Evidence for Atomic Defects in Graphene Layers. *Nature* **2004**, *430*, 870–873.
68. Meyer, J. C.; Kisielowski, C.; Erni, R.; Rossell, M. D.; Crommie, M. F.; Zettl, A. Direct Imaging of Lattice Atoms and Topological Defects in Graphene Membranes. *Nano Lett.* **2008**, *8*, 3582–3586.